Cengiz Baykasoglu[1]
Department of Mechanical Engineering,
Hitit University,
Corum 19030, Turkey
e-mail: cengizbaykasoglu@hitit.edu.tr

Oncu Akyildiz
Department of Metallurgical
and Materials Engineering,
Hitit University,
Corum 19030, Turkey
e-mail: oncuakyildiz@hitit.edu.tr

Duygu Candemir
Department of Metallurgical
and Materials Engineering,
Hitit University,
Corum 19030, Turkey
e-mail: duygukorsacilar@hitit.edu.tr

Qingcheng Yang[2]
Department of Mechanical Engineering
and Materials Science,
University of Pittsburgh,
Pittsburgh, PA 15261
e-mail: qzy25@psu.edu

Albert C. To[1]
Department of Mechanical Engineering
and Materials Science,
University of Pittsburgh,
Pittsburgh, PA 15261
e-mail: albertto@pitt.edu

Predicting Microstructure Evolution During Directed Energy Deposition Additive Manufacturing of Ti-6Al-4V

Laser engineering net shaping (LENS) is one of the representative processes of directed energy deposition (DED) in which a moving heat source having high-intensity melts and fuses metal powders together to print parts. The complex and nonuniform thermal gradients during the laser heating and cooling cycles in the LENS process directly affect the microstructural characteristics, and thereby the ultimate mechanical properties of fabricated parts. Therefore, prediction of microstructure evolution during the LENS process is of paramount importance. The objective of this study is to present a thermo-microstructural model for predicting microstructure evolution during the LENS process of Ti-6Al-4V. First, a detailed transient thermal finite element (FE) model is developed and validated for a sample LENS process. Then, a density type microstructural model which enables calculation of the α-phase fractions (i.e., Widmanstätten colony and basketweave α-phase fractions), β-phase fraction, and alpha lath widths during LENS process is developed and coupled to the thermal model. The microstructural algorithm is first verified by comparing the phase fraction results with the results presented in the literature for a given thermal history data. Second, the average lath width values calculated using the model are compared with the experimentally measured counterparts, where a reasonable agreement is achieved in both cases. [DOI: 10.1115/1.4038894]

1 Introduction

Additive manufacturing (AM) provides an unprecedented opportunity to produce near-net-shape metal parts through layer-by-layer addition of materials and offers a number of advantages over traditional manufacturing methods [1]. Two main AM process categories used for manufacturing metallic parts are directed energy deposition (DED) and powder bed fusion. Both categories share the similar aspect that a high intensity energy source is used to heat and melt powder material, which solidifies to form a fully dense layer. The main difference between these categories is in the powder feed system. In a typical powder bed fusion process, the energy source melts the metal powders raked into flat layer in a powder bed, whereas in a typical DED process the metal powders are coaxially fed with the energy source. Our focus in this study is on laser engineering net shaping (LENS) process, which is one of the successful commercial forms of DED [2–4]. For further information on the metal-based AM processes, materials, and mechanisms, interested readers can see the excellent review papers [1,5,6].

Although metal AM has the several advantages, some technical challenges associated with achieving the desired mechanical properties of the printed parts are still preventing the use of metal AM technologies in a broad range of industrial applications [7]. At this point, several factors, such as quality of powder feedstock, existence of porosity, incomplete and overmelting, balling and microstructural characteristic, directly affect the final mechanical properties of AM parts [8–14]. At the optimal build conditions, in which most of the aforementioned factors are controlled, the microstructural features represent the ultimate factor that dictates the mechanical properties of the metal AM parts [11–13]. Hence, understanding how the AM process affects the part microstructure is of critical importance. Once the microstructure can be controlled during AM process, manufacturing parts with locally tailored mechanical properties would be possible.

The microstructural characteristics of Ti-6Al-4V parts strongly depend on the thermal history during the DED process, which generally includes high and nonuniform thermal gradients [14,15]. Hence, accurate prediction of thermal history during the DED process is of paramount importance. The utilization of finite element (FE) based macroscale modeling technique is suitable for modeling the thermal interactions during DED processing of industrial parts [9]. These modeling techniques generally focus on the overall thermal behavior in that several physical phenomena that occur during the DED processing (i.e., laser/powder interactions, melt pool/laser interaction, and melt pool/powder interaction) are lumped together and represented using simplified models due to modeling difficulties (i.e., mismatches in temporal and spatial scales and excessive computational cost) [16,17]. Most of the FE models employed in DED process modeling are inspired by the welding mechanics simulation in which the fluid flow and

[1]Corresponding authors.
[2]Present address: Department of Materials Science and Engineering, Penn State University, N-257 Millennium Science Complex, State College, PA 16802.

Manuscript received September 25, 2017; final manuscript received December 20, 2017; published online February 23, 2018. Assoc. Editor: Zhijian J. Pei.

physics of the heat generation are ignored, while the melt pool is treated as a soft solid and heat input models are used to describe laser heat source [18–21]. Significant research effort has been devoted to modeling heat transfer in metal deposition using FE-based modeling techniques [16,17,21–35].

The density type modeling approach, also called internal state variable approach [36], for microstructure evolution during processing such as welding, laser forming, and metal deposition is generally preferred, since it could be directly coupled with thermal FE models and requires relatively less computational cost. In this approach, density fields such as phase fractions of different phases are computed at the integration points of finite elements [12,17]. In this study, we considered the well-known titanium alloy called Ti-6Al-4V. Ti-6Al-4V is a dual phase heat treatable alloy and contains approximately 90% α-phase at room temperature and 100% fully stable β-phase above β-transus temperature ($T_\beta^{\text{trans}} \cong 1000\,^\circ\text{C}$) [37]. On the other hand, the morphology of $(\alpha+\beta)$-phase varies significantly depending on the thermal and mechanical conditions during the heating and cooling cycles in DED processes [14]. During heating, α-phase transforms to the β-phase up to β-transus temperature. Upon cooling back to room temperature, if cooling rate is high, diffusionless transformation takes place and the β-phase transforms back to massive and martensitic α-phases. Alternatively, diffusion controlled phase transformation occurs at low cooling rates and allotriomorphic or grain boundary α may grow at the β-boundaries and then, plate-like α-phases grow first by starting from the grain boundary α phase within the remaining β-phase [38–40]. The plate-like α-phases are also called Widmanstätten α and can be divided into colony and basketweave morphologies based on an intragranular nucleation temperature.

The kinetics of the diffusional transformations under isothermal conditions have been successfully described with the Johnson–Mehl–Avrami–Kolmogorov (JMAK) equation [41–43] for Ti-6Al-4V [44]. Since JMAK's equation can be applied only to the isothermal transformation process, Scheil's [45] or Christian's [46] additivity rules have been widely used to describe the nonisothermal cooling process together with JMAK equation. On the other hand, martensitic transformation for Ti-6Al-4V is still poorly understood and the Koistinen and Marburger equation [47] has been widely used for this transformation [48,49]. In addition, dissolution kinetics of the α-phases to the β-phase during the heating cycles have been studied by a few authors [38–40,50] by using JMAK equation and/or as one-dimensional plate growth of the β-phase which assumes a parabolic β growth rate [38,51–53]. Relevant FE-based thermo-kinetic studies that couple heat transfer models with phase transformation kinetics using these approaches are summarized as follows. Kelly [38] and Kelly and Kampe [39,40] carried out an extensive experimental and numerical investigation focusing on microstructure evolution of Ti-6Al-4V during the LENS process by using two-dimensional finite difference formulation which considers colony and basketweave Widmanstätten α-phases. Charles [51] and Charles and Järvstråt [52] developed thermo-microstructural FE-based models to examine microstructural evolution of weld deposited Ti-6Al-4V by using the similar kinetic model as in Refs. [38–40]. However, they included martensitic transformation and α-lath width in their model. In a later work, Murgau et al. [53] improved the previous kinetic model in Refs. [51] and [52] by extending their kinetics formulations and presented a comprehensive microstructural model for Ti-6Al-4V. The grain boundary alpha phase transformation is included in the model separately, and the colony and basketweave alpha phases are considered as the same Widmanstätten phase as in Ref. [53]. Fan et al. [54] investigated the phase transformations during laser forming of Ti-6Al-4V using FE method. The laser forming process includes only a single laser pass, and the proposed model in Ref. [54] is relatively less complex than multilayer metal deposition process. Crespo and Vilar [55] and Crespo [56] developed FE-based thermo-kinetic models that coupled heat transfer calculations with phase transformation kinetics and microstructure-property relations, and examined the microstructural characteristics during the laser powder deposition of Ti-6Al-4V. Similarly, Suárez et al. [57] developed a transient thermo-metallurgical FE model for simulation of the deposition of Ti-6Al-4V, which follows similar methodology implemented for weld deposited Ti-6Al-4V by Charles and Järvstråt [52]. Vastola et al. [12] introduced a FE-based model for predicting microstructural evolution during electron beam melting and selective laser melting. Later, Irwin et al. [58] presented an implementation of Kelly's microstructural model [38–40] and Charles' lath width model [51] for predicting microstructure from thermal history during AM of Ti-6Al-4V.

The aforementioned studies demonstrated that macroscale modeling is a powerful tool for predicting the thermal history and microstructural evolution during metal deposition processing. Although the thermal modeling of DED process has been studied extensively, there are limited studies on FE-based three-dimensional thermo-kinetics modeling of LENS process. In addition, few studies contain detailed kinetic models. Motivated by these facts, a detailed three-dimensional thermo-microstructural model is presented here by taking into account the most recent observations and modeling techniques in the literature [38,51–53,55,56,58]. The microstructural model is mainly based on Kelly's and Charles' microstructural models [38,51], which enable the calculation of α-phase fractions, β-phase fraction, and alpha lath width during the LENS process.

2 Numerical Model

The overall procedure for predicting the temperature history and volume fraction of each phase is shown in Fig. 1. Note that stress-induced phase transformations are ignored since the thermal-driven phase changes during the metal deposition processes have dominant effects [17,58]. Similarly, the effects of mechanical deformations on thermal behavior (i.e., plasticity induced thermal dissipation, change in the thermal boundary conditions) are not taken into account in the modeling due to their low contributions to the thermal evolution [17,59]. In addition, the effects of microstructure on thermal properties of material are not directly modeled. Commercially available FE software ABAQUS is used to implement the model and perform the simulations. In order to define heat source input and calculate microstructural features, two subroutines (i.e., DFLUX and USDFLD) are written using FORTRAN and included in the model. As can be seen from Fig. 1, at each time increment, thermal outputs at the integration points are computed first and then, microstructural outputs are computed and stored via user subroutine. After each time-step, the definition of the heat source and the corresponding model data are updated by considered details given in Secs. 2.1 and 2.2, and simulation continues until the LENS process is completed.

The geometric and process parameters are selected as the same as the proposed parameters in our previous study [33] in order to utilize previous experimental thermal measurement results and

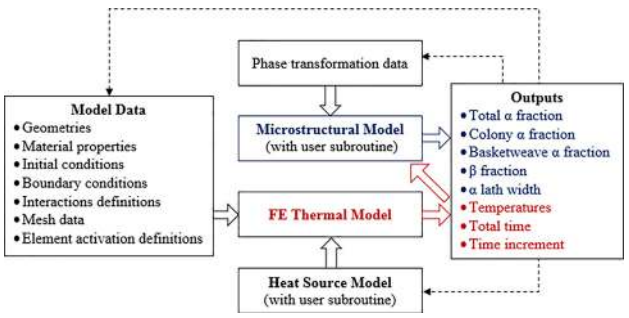

Fig. 1 The overall procedure for prediction of the thermal and microstructural outputs

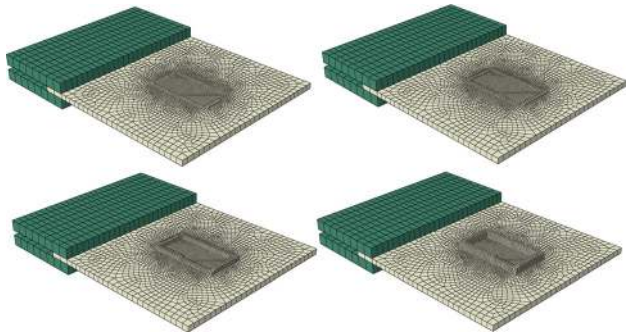

Fig. 2 Illustration of deposition process

manufactured rectangular-shaped Ti-6Al-4V specimen composed of five layers (Fig. 2). The longer length, shorter length, height, and width of the deposition are 41.86 mm, 22.37 mm, 4.43 mm, and 2.72 mm, respectively. A Ti-6Al-4V square substrate with the width of 101.6 mm and the thickness of 3.18 mm, and an aluminum fixture with the length of 50.8 mm, width of 101.6, and height of 6.35 mm are used in simulation and experimental validation. The deposition starts at the lower right corner of the rectangular-shaped part and then continued counter-clockwise direction (i.e., Fig. 2). Each deposition layer is chosen as one element tall and two element wide, as proposed in Refs. [30] and [32] and in our previous study [33] in which a mesh sensitivity analysis was performed for a similar thermal problem. In addition, a finer mesh is used in the deposition and its proximity to improve accuracy. Eight-node brick elements are employed in simulation and the FE model contains 4609 elements and 8722 nodes.

The material deposition during the LENS process is modeled using inactive/active element approach similar to the approaches in Refs. [21] and [30]. In this approach, the unique mesh of both the substrate and the entire metal deposition are first generated using a mesh generator and then, an activation time-step for each deposition track element is defined according to the input geometric dimensions and process parameters. Thus, at the beginning of the first step in the simulation, all elements of the metal deposition are made inactive in order to render them thermally dormant, while still keeping them attached together. Once an element is activated, the degrees-of-freedom and the new external surface of the active element are included in the simulation. At this point, the "model change" option in ABAQUS is used to define the element activation process. The total metal deposition process including final cooling step lasts 1600 s in which the laser deposition steps (i.e., heating steps) takes 293.9 s. The model consists of 1002 time-steps including element activation, heating, and final cooling steps. Note that a very small time-step of 1×10^{-8} s is first defined for element activation and then, heating time steps are defined after each activation step in order to simulate the thermal interactions. The minimum and maximum increment sizes are defined as 1×10^{-5} and 0.1 s for heating and cooling steps. It is observed that an average of six iterations per heating time-step is required to achieve convergence. Figure 2 shows the snapshots from the element activation process.

2.1 Thermal Model. The governing energy balance equation of heat transfer can be expressed as

$$\rho C_p \frac{dT(\mathbf{x},t)}{dt} = -\nabla \cdot \mathbf{q}(\mathbf{x},t) + Q(\mathbf{x},t) \tag{1}$$

in any subvolume V of the evolving AM part. Here, T denotes temperature, ρ is the material density, C_p is the temperature-dependent specific heat, t is the time, $\mathbf{x}$ is the spatial coordinate, $\mathbf{q}$ is the heat flux vector, and Q is the body heat source. The heat flux vector $\mathbf{q}$ is given by Fourier's conduction law

$$\mathbf{q} = -k(T)\nabla \mathrm{T}(\mathbf{x},t) \tag{2}$$

where k is the temperature-dependent thermal conductivity. We considered the temperature-dependent thermal properties of Ti-6Al-4V given in Refs. [30], [32], and [33] for LENS process (Table 1). The thermal properties of Ti-6Al-4V above 870 °C are assumed to be constant. In addition, the density of Ti-6Al-4V is assumed to be a constant value of 4.43×10^3 kg/m^3 similar to the assumption in Refs. [21], [30], [32], [33], and [54].

Table 1 Temperature-dependent thermal properties of Ti-6Al-4V [21,32,33]

T (°C)	k (W/m/°C)	C_p (J/kg/°C)
20	6.6	565
93	7.3	565
205	9.1	574
250	9.7	586
315	10.6	603
425	12.6	649
500	13.9	682
540	14.6	699
650	17.5	770
760	17.5	858
800	17.5	895
870	17.5	959

The physics of the heat generation, fluid flow, and heat transfer in the melt pool are not directly simulated in this study. Their effects are introduced into the simulation by using Goldak's double ellipsoid heat source model [60]. This model has been widely used to describe the laser heat source term during LENS process [30,32,33,38] and is defined as

$$q(x',y',z') = \frac{6\sqrt{3}P\eta f}{abc\pi^{3/2}} e^{\left(-3\frac{x'^2}{a^2}-3\frac{y'^2}{b^2}-3\frac{z'^2}{c^2}\right)} \tag{3}$$

where P is the laser power; η is the absorption efficiency; f is the scaling factor; x', y', and z' are the local coordinates with the origin centered at where the moving heat source with scan speed v reaches the maximum value; and a, b, and c are the transverse, depth, and longitudinal semi-axes of the ellipsoid, respectively (see Fig. 3). Different values can be used to define the rear and front of the longitudinal ellipsoid axis c. On the other hand, the effect of heat source on the top surface of each deposition track is generally considered to be circular in the LENS process since the laser beam is moving slowly [30,32,33]. Hence, both a and c are generally taken as half of deposition track width and b to the melt pool depth. On the other hand, the melt pool depth to radius ratio (i.e., b/a or b/c)

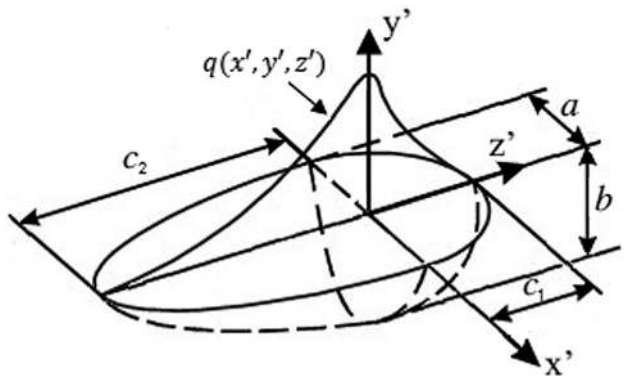

Fig. 3 Double ellipsoid heat source model

is generally taken as 0.6 [30,32]. By using the above definitions and assumptions, the values used here are $P = 300$ W, $\eta = 0.45$ [30], $v = 2$ mm/s, $a = 1.36$ mm, $b = 0.816$ mm, $c = 1.36$ mm, and $f = 1$. Note that "DFLUX" user subroutine in ABAQUS is used to specify distributed volumetric heat sources similar to the one in Ref. [26].

The initial temperature field in the entire volume is given by

$$T(\mathbf{x}, t_0) = T_0(\mathbf{x}) \tag{4}$$

where T_0 is the prescribed initial temperature. The surface heat losses due to convection and radiation are given, respectively, as

$$q_{\text{conv}}(\mathbf{x}, t) = h(T - T_\infty) \tag{5}$$

$$q_{\text{rad}}(\mathbf{x}, t) = \varepsilon\sigma(T^4 - T_\infty^4) \tag{6}$$

where h is the convection coefficient, T_∞ is the environment temperature, ε is the emissivity, and σ is the Stefan–Boltzmann constant. Forced and free convection models are proposed in this study. During the heating process, the average forced convection coefficient $h = 55$ W/m^2/°C [33] is used, while the free convection coefficient $h = 10$ W/m^2/°C [32] is applied after heating process because the argon atmosphere is no longer available and convection becomes uniform on all surfaces. The initial and ambient temperatures are fixed to 27 °C. The emissivity is temperature independent and set to 0.54 [32].

2.2 Microstructural Model. The microstructure of the solid state Ti-6Al-4V titanium alloy is modeled using the volumetric phase fractions [51–59] by considering only the Widmanstätten colony and basketweave α-phase fractions during the diffusion controlled transformation of the β-phase due to the negligible grain boundary α phase fractions [38]. The massive and martensitic transformations are not included in the microstructural model due to several reasons. First, these transformations are poorly understood and there is a wide discrepancy in the cooling rate above in which fully or partially diffusionless transformation takes place (5.1–410 °C/s) [49,61] and martensite start temperature (575–800 °C) data [34,38,54–56]. These discrepancies possibly emerge due to a lack of standard test method to distinguish and quantify the amount of martensite alpha phase fractions in a specimen. Particularly, distinguishing martensite fraction is very challenging as hexagonal close-packed martensitic and basketweave morphologies have similar appearances and have comparable lattice constants [50,58]. Second, most of the microstructural

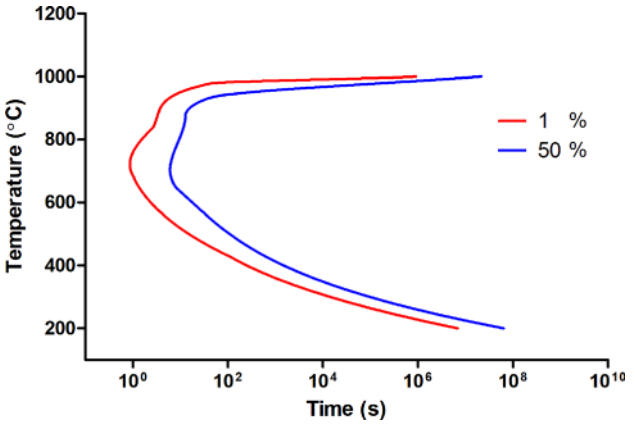

Fig. 5 Time–temperature–transformation diagram for α-phases. The diagram is based on the calculations presented in Ref. [38] and plotted by using the piecewise polynomials reported in Ref. [53].

models that consider the martensitic transformation assume cooling rates faster than 410 °C/s [34,54–56,62]. For the process parameters used in this work, the cooling rates below martensite start temperature do not exceed 410 °C/s during deposition.

When computing volumetric phase fractions, the very same model logic presented in Refs. [38], [52], [53], and [58] is adopted and is shown schematically in Fig. 4. Accordingly, if the current β-phase fraction, X_β, is above its equilibrium value, X_β^{eq}, it decomposes into α phase. This is true when the temperature goes below T_β^{trans} and the cooling rate is low enough to allow diffusional transformations. The transformed α volume fraction cooling is calculated using the JMAK equation

$$X_\alpha = (1 - \exp(-k_{\beta\alpha}\tau^{N_{\beta\alpha}}))X_\alpha^{\text{eq}} \tag{7}$$

Here, X_α is the calculated fraction of α-phases, $k_{\beta\alpha}$ and $N_{\beta\alpha}$ are material parameters that can be extracted from the time–temperature–transformation diagrams given in Fig. 5. τ is a relative time measured from the start of the transformation and X_α^{eq} is the equilibrium fraction of the α-phase that can be modeled as a function of temperature as follows:

$$X_\alpha^{\text{eq}}(T) = 0.91(1 - 1/\exp(0.013(T_\beta^{\text{trans}} - T))) \tag{8}$$

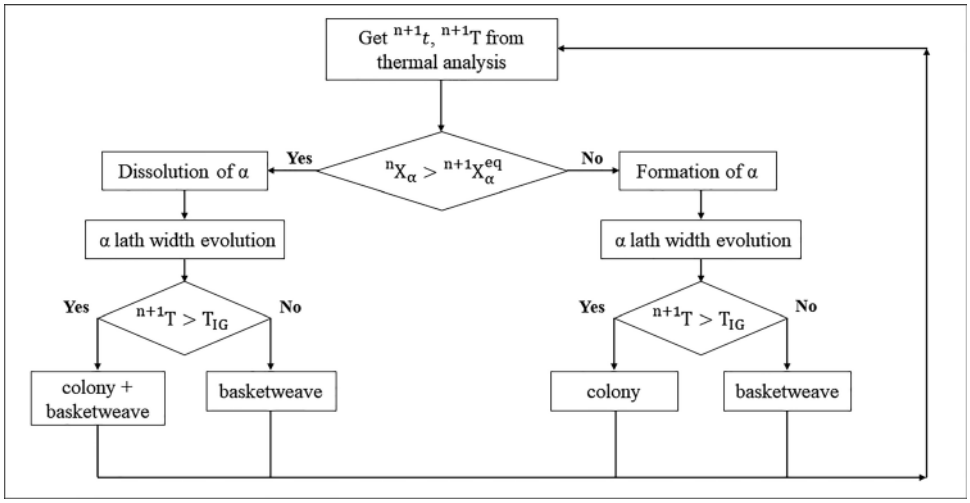

Fig. 4 Flowchart for the microstructural model

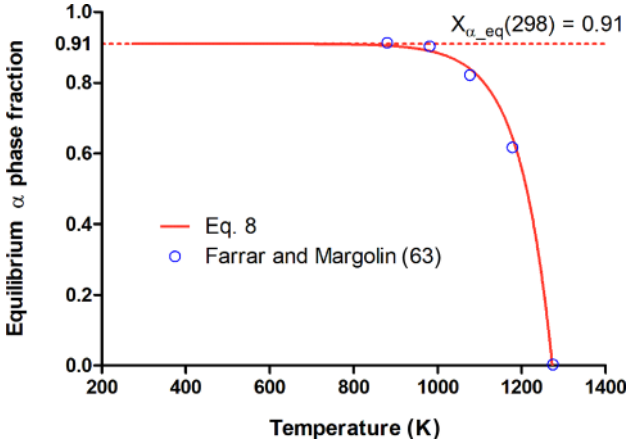

Fig. 6 Equilibrium α-phase fraction as a function of temperature given by Eq. (8) and experimental values from Ref. [63]

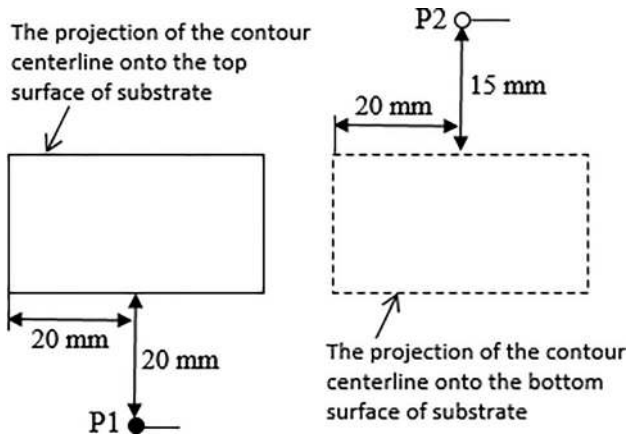

Fig. 7 Thermocouples measurement points on the top and bottom surfaces of substrate

Equation (8) is plotted in Fig. 6 where the coefficients 0.91 and 0.013 are found to give the best agreement with the experimental data presented in Ref. [63].

A discrete formulation of Eq. (7) is used to update the value of the volumetric phase fractions of α phase at time $n+1$

$$ {}^{n+1}X_\alpha = {}^{n}X_\alpha + \Delta X_\alpha = (1 - \exp(-k_{\beta\alpha}(t_c + \Delta t)^{N_{\beta\alpha}}))^{n+1}X_\alpha^{\text{eq}} \quad (9) $$

Here, t_c is a fictitious time defined to adopt the principle of additivity; a time that would have taken to reach the current concentration if the current temperature is taken as constant throughout the transformation [53]

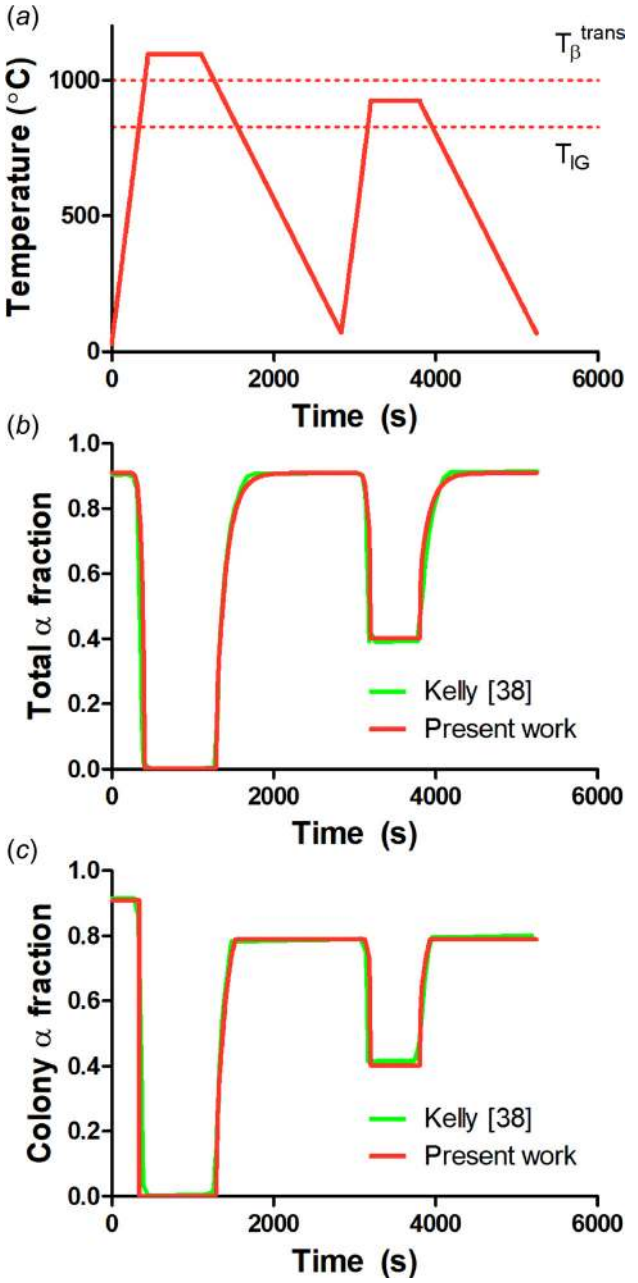

Fig. 9 (*a*) The primary and secondary heat treatment curve given by Kelly [38] and ((*b*) and (*c*)) corresponding α phase fractions and computed phase fractions in the present work using the same temperature–time data

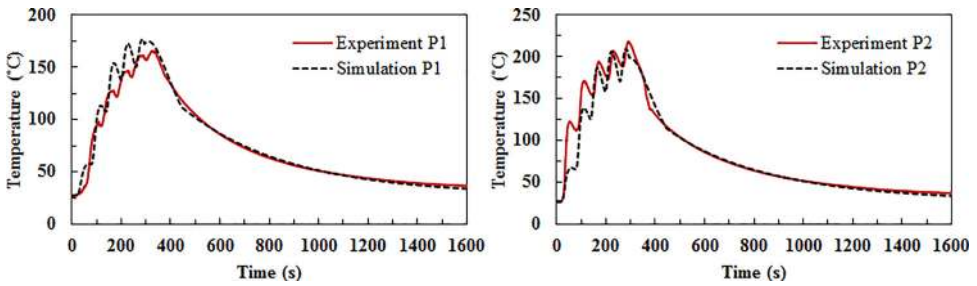

Fig. 8 Temperature history comparison between the simulation and experimental measurements at P1 and P2

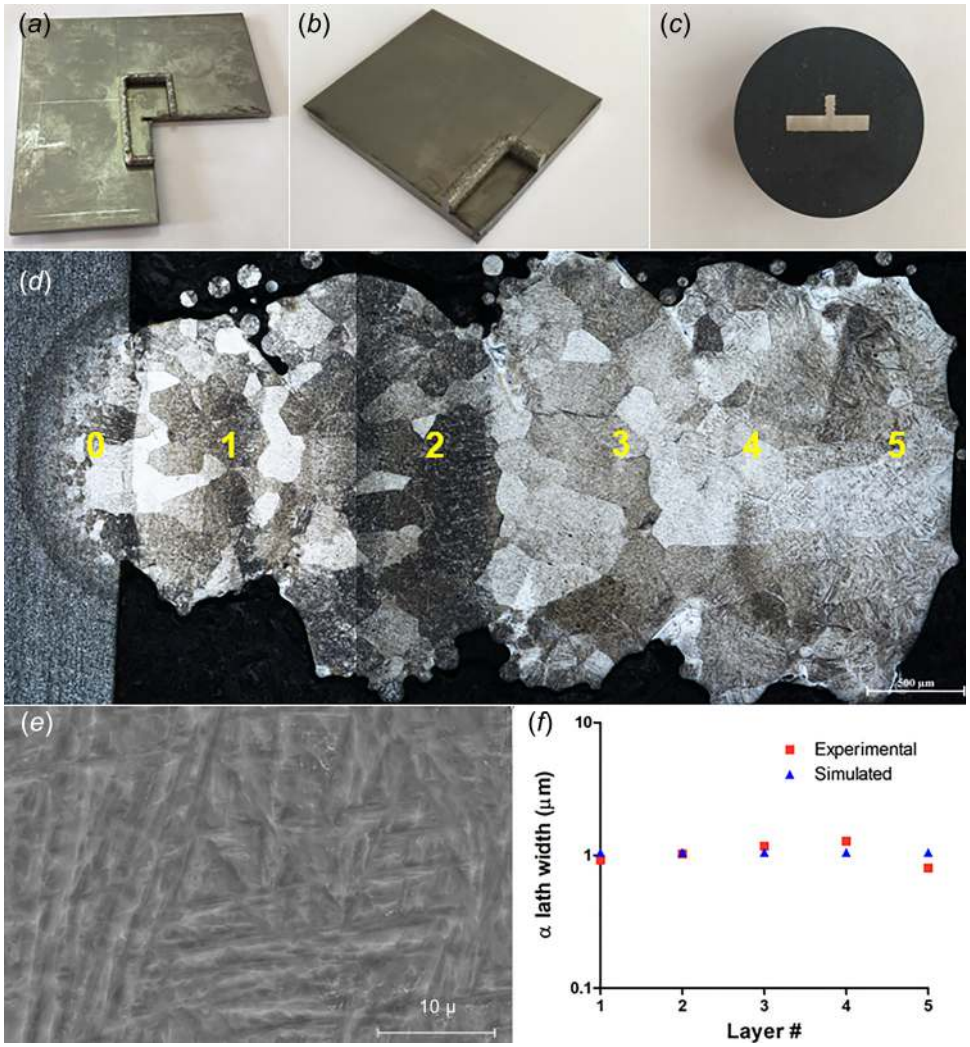

Fig. 10 The microstructure of the five-layer LENS deposited sample: (*a*)–(*c*) preparation of the sample, (*d*) optical microscopy, (*e*) a representative SEM micrograph showing α laths, and (*f*) experimental and simulated average lath widths versus layer number

$$t_c = \left(-\ln\left(1 - \frac{{}^{n}X_{\alpha}}{{}^{n+1}X_{\alpha}^{\mathrm{eq}}}\right) \Big/ k_{\beta\alpha} \right)^{\frac{1}{N_{\beta\alpha}}} \tag{10}$$

The α phase fraction is further divided into the colony—α fraction $X_{C-\alpha}$ and the basketweave—α fraction $X_{\mathrm{BW}-\alpha}$ depending on the intragranular nucleation temperature ($T_{\mathrm{IG}} = 827\,^{\circ}\mathrm{C}$)[38]. If the current temperature is greater than T_{IG} the transformed α becomes part of the colony; otherwise, it becomes basketweave morphology [58]. The necessary condition at each time-step is $X_{\alpha} = X_{C-\alpha} + X_{\mathrm{BW}-\alpha}$.

During heating, the dissolution of alpha phase is considered using a parabolic β growth rate function proposed by Kelly [38]

$${}^{n+1}X_{\alpha} = \begin{cases} 1 - {}^{n+1}X_{\beta}^{\mathrm{eq}} f_{\mathrm{diss}}(T)\sqrt{(t^* + \Delta t)} & 0 < t^* + \Delta t < t_{\mathrm{crit}} \\ 1 - {}^{n+1}X_{\beta}^{\mathrm{eq}} & t^* + \Delta t > t_{\mathrm{crit}} \end{cases} \tag{11}$$

Here, t^* is the fictitious time as in the JMAK model and t_{crit} is the time for which the transformation reaction is equal to 1

$$t^* = \left(\frac{{}^{n}X_{\beta}}{{}^{n+1}X_{\beta}^{\mathrm{eq}} f_{\mathrm{diss}}(T)} \right)^2 \tag{12}$$

$$t_{\mathrm{crit}} = \left(\frac{1}{f_{\mathrm{diss}}(T)} \right)^2 \tag{13}$$

$$f_{\mathrm{diss}}(T) = 2.2 \times 10^{-31} T^{9.89} \tag{14}$$

During heating, whether the dissolved α is taken from the colony or basketweave morphology depends on the intragranular nucleation temperature. If the current temperature is less than T_{IG}, then only the basketweave morphology dissolves; otherwise, both basketweave and colony dissolve proportionally according to the following equations [38]:

$${}^{n+1}X_{C-\alpha} = \frac{{}^{\mathrm{TIG}}X_{C-\alpha}}{{}^{\mathrm{TIG}}X_{\alpha}} {}^{n+1}X_{\alpha} \tag{15}$$

$${}^{n+1}X_{\mathrm{BW}-\alpha} = \frac{{}^{\mathrm{TIG}}X_{\mathrm{BW}-\alpha}}{{}^{\mathrm{TIG}}X_{\alpha}} {}^{n+1}X_{\alpha} \tag{16}$$

where ${}^{\mathrm{TIG}}X_{C-\alpha}$, ${}^{\mathrm{TIG}}X_{\mathrm{BW}-\alpha}$, and ${}^{\mathrm{TIG}}X_{\alpha}$ are the colony, basketweave, and total α fractions at T_{IG}, respectively.

The α lath width evolution is also modeled using the approach presented by Charles and Järvstråt [52]

$${}^{n+1}w = ({}^{n}w {}^{n}X_{\alpha} + w^{\mathrm{eq}} \Delta X_{\alpha}) / {}^{n+1}X_{\alpha} \tag{17}$$

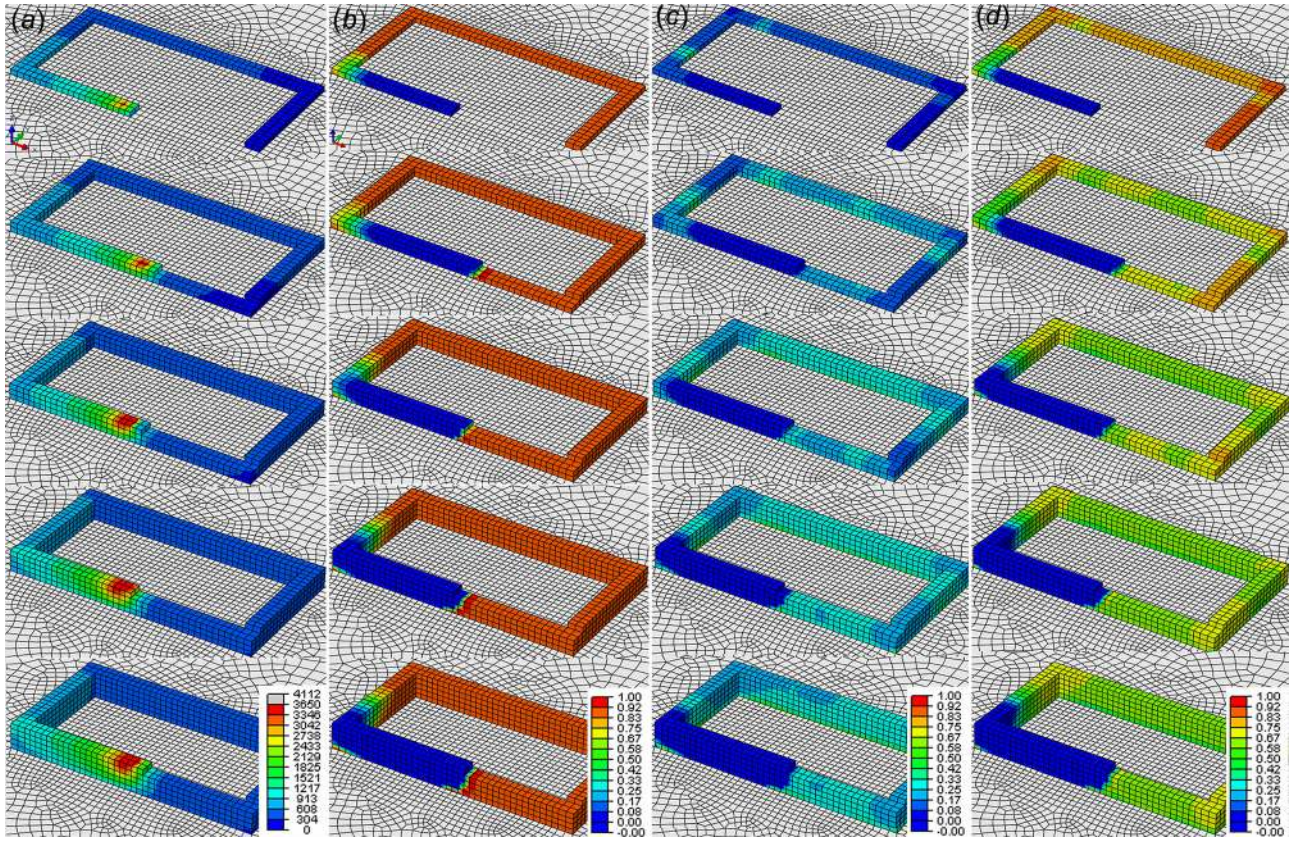

Fig. 11 (*a*) Temperatures in Celsius, (*b*) total—α, (*c*) colony—α, and (*d*) basketweave—α phase fractions evolution during layer-by-layer deposition

Here, ${}^{n}w$ is the lath width from the previous time-step and ΔX_α is the change in α fraction. The equilibrium value of α lath width, w^{eq}, is calculated using an Arrhenius equation with recently reported prefactor, $k_w = 1.42\mu$m, and an activation temperature, $T_{\text{act}} = 294$K [58]

$$w^{\text{eq}} = k_w \exp\left(-\frac{T_{\text{act}}}{{}^{n}T}\right) \tag{18}$$

3 Results and Discussion

The transient thermal FE model is first validated using experimental measurement results which have been used in our previous study [33]. In the experiment, rectangular contours of Ti-6Al-4V are produced using the Optomec LENS system (Fig. 10). The laser power is selected as 300 W with beam intensity of 18,679 MW/m^2 and minimum spot size of 143 μm at focus. The travel speed is 2 mm/s with a powder feed rate of 8.6 g/min. On the other hand, two Omega SA1XL-K-72 thermocouples are attached at the top and bottom surfaces of the substrate in order to collect the temperature data during heating and cooling processes. Time and temperature data are recorded at a sampling rate of 100 Hz. The locations of thermocouples are geometrically shown in Fig. 7, where solid circle (point 1, P1) denotes the top surface while empty circle (point 2, P2) represents the bottom surface.

The numerical temperature data are also obtained at the same thermocouple locations. Figure 8 shows the temperature comparison between experimental measurement and FE analysis results. As can be seen in the figure, both experimental and numerical results follow very similar trend during the heating process and they have almost the same trend after the heating process (i.e., during cooling process). Higher temperature values are observed at P2 compared to P1 especially during heating cycles since P2 is closer to the heat effected area than P1. Note that the FE temperature results at both P1 and P2 are in good agreement with experimental thermocouple measurements which also show the validity of the proposed FE model through the thickness direction.

The microstructure model is first verified using the primary and secondary heat treatment curves and the corresponding phase fraction evolutions given in Kelly's original implementation [38]. At this point, the microstructural model is tested for two different cooling rates (0.6 and 10 °C/s). Figure 9 shows the phase fraction evolution comparison between our simulation results and results in the reference work of Kelly [38] for cooling rate of 0.6 °C/s. As can be seen in Fig. 9, the total α phase fractions in both results return to about 91% shortly after dissolution temperature and have almost the same trends during heating and cooling cycles. In addition, the colony α phase fraction results are also in good agreement with Kelly's original implementation during both the primary and secondary heat treatment processes. Note that the similar agreement is also observed for the cooling rate of 10 °C/s (Fig. 7.24 of Ref. [38]) which are not presented to save space.

For experimental validation, cross sections for microstructural analysis are cut from the LENS deposited sample utilized as in Ref. [33] (Fig. 10). The cross sections are mounted in round bakelite (Metkon-Phenolic resin powder) with a diameter of 4 cm and subjected to mechanical grinding with 180–1200 grit SiC paper followed by polishing with 6 μm and 1 μm diamond suspensions to mirror finish (Metkon Forcipol 1V Grinder-Polisher). Finally, the samples are etched with Kroll's reagent (%2 HF and %6 HNO_3 within distilled water) and cleaned using ethanol. Microstructure of the samples is investigated by using optical microscope (Nikon ECLIPSE LV150N) and scanning electron microscope (SEM) in 3000× and 5000× magnifications (FEI/Quanta 450 FEG) for measuring lath widths in each layer.

The polycrystalline structure at each layer is clearly shown in Fig. 10(*d*). Experimental α lath widths are measured from SEM

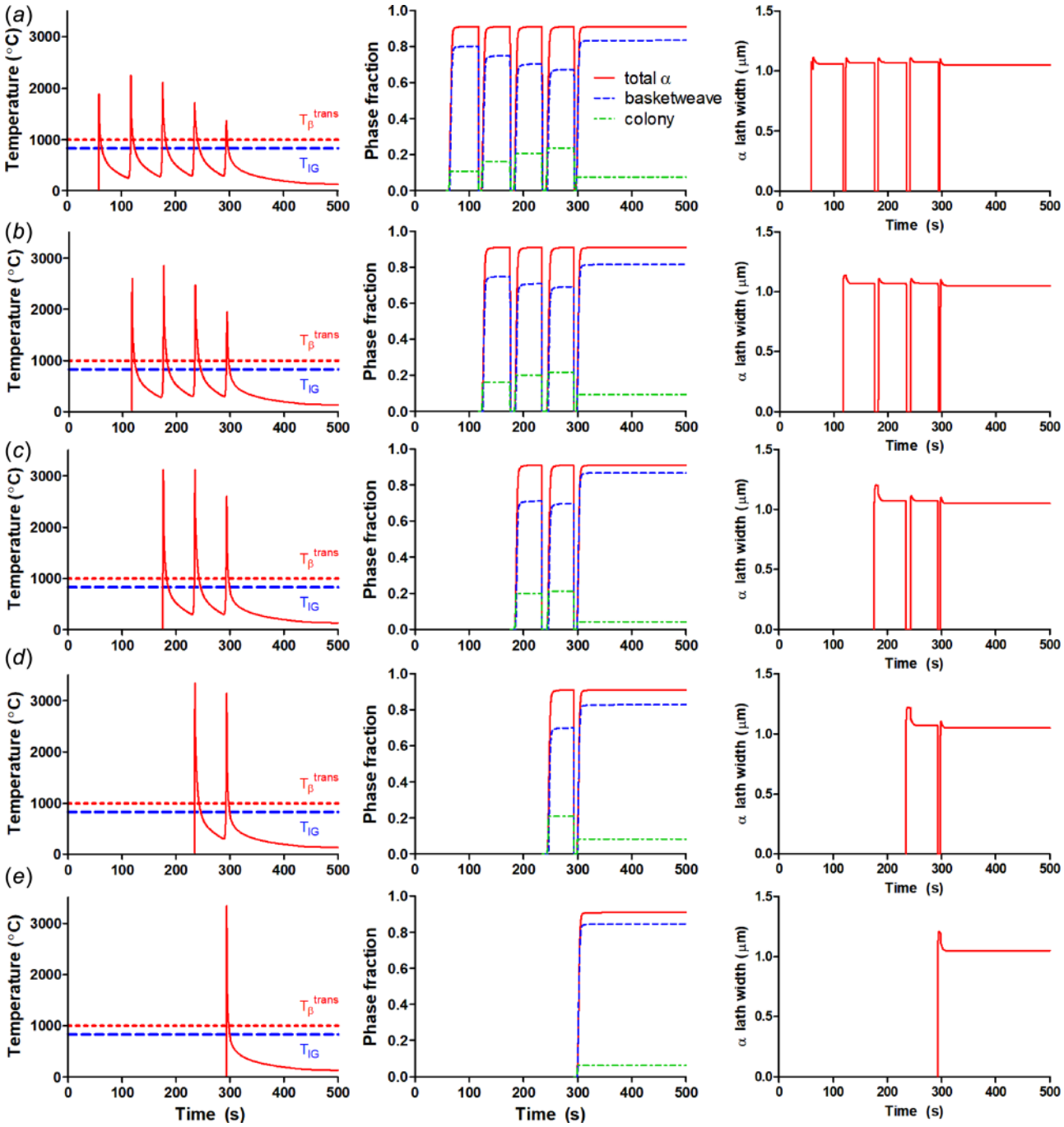

Fig. 12 Temperature, alpha phase fractions, and lath width evolution for the points probed from successive layers, layers 1–5 in (*a*)–(*e*), starting from the base point A (at the first layer) shown in Fig. 13

micrographs of each layer using the IMAGEJ software [64] and taking their arithmetic mean. Similarly, the α lath widths at the end of the simulation are collected from all integration points within each layer and averaged. Results for each layer are shown in Fig. 10(*f*) in comparison with SEM measurements. As can be seen in Fig. 10, the microstructural model results are in good agreement with experimental measurements. The prediction of α lath width as shown in Fig. 10 allows for the prediction of mechanical properties without requiring destructive testing. Lath width is closely linked to hardness, with thicker laths generally correlating to lower hardness [58].

The simulated process as well as temperature, total—α, basketweave—α and colony—α phase fraction profiles are given in Fig. 11 at different time steps corresponding to each layer of the rectangular contour.

After cooling to room temperature, the total α-phase fractions return to the equilibrium value of $X_\alpha = 0.91$, where β-phase regions close to the heat source are shown in Figs. 11(*b*)–11(*d*). Note that the phase fraction results are only computed at the integration points of the element and the results are interpolated linearly between layers. Hence, the resolution can be improved by increasing the number of elements for modeling one layer. Figure 12 shows outputs for the points probed from successive layers starting from the base point A (at the first layer) shown in Fig. 13.

After its deposition, point A has experienced four heating and cooling cycles as shown in Fig. 12(*a*). In each step, primary

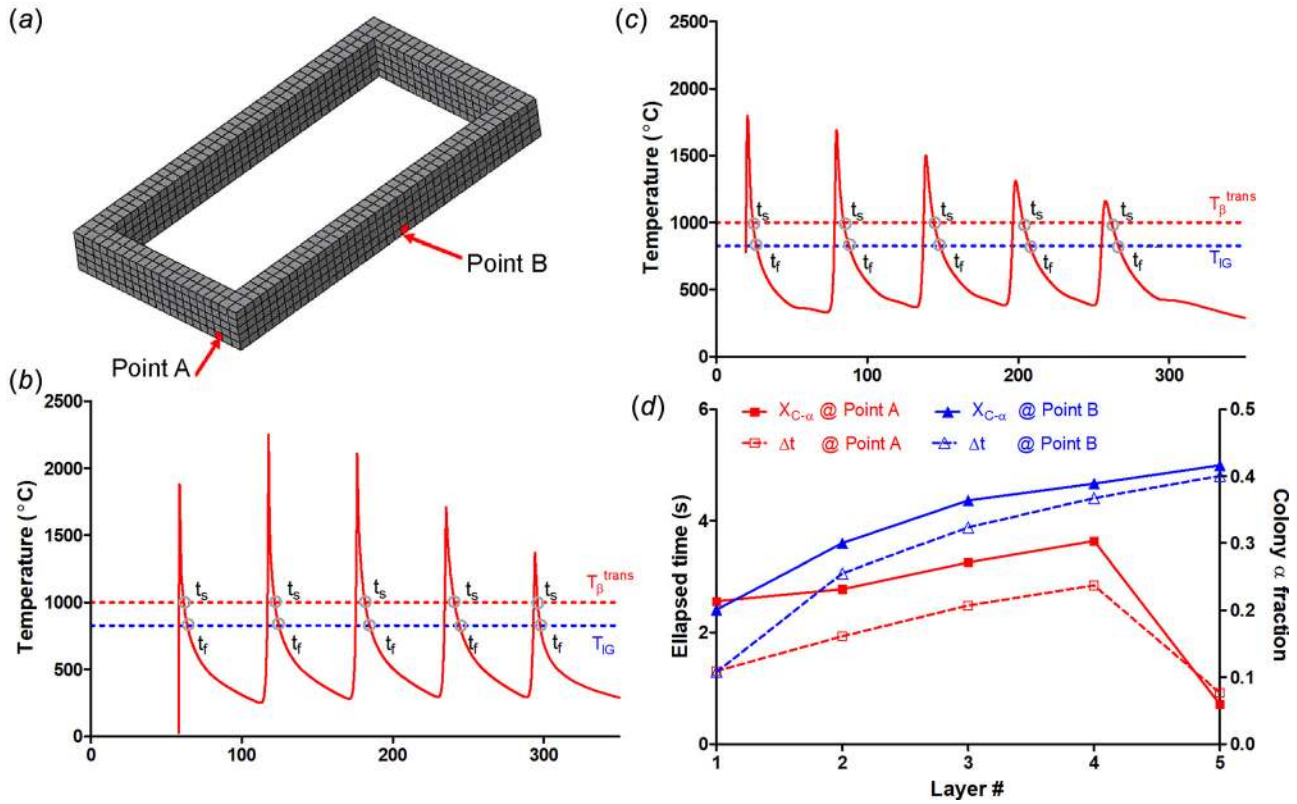

Fig. 13 (*a*) Position of probed points, (*b*) temperature profiles for point A, (*c*) point B, and (*d*) time elapsed ($\Delta t^i = t_f^i - t_s^i$) during $\beta \rightarrow$ colony—α transformation and corresponding colony—α fraction formed

heating or heating above T_β^{trans} takes place. Before the first reheating, it has 11% colony—α at equilibrium as can be seen from Fig. 12(*a*). This amount continues to increase to approximately 24% before the last reheating step, where it decreases to 8% colony—α afterward. Very similar trend is observed in other layers, which is closely related to the time elapsed during cooling from T_β^{trans} to T_{IG}. In order to show this correlation, start and finish times for colony—α formation during each cooling cycle are marked in Fig. 13(*b*), and time elapsed ($\Delta t^i = t_f^i - t_s^i$) during $\beta \rightarrow$ colony—α transformation at each cooling step and its relation to colony—α fractions is presented in Fig. 13(*d*).

Note that point A is the last deposition point on layer 1, and there is no temperature data until it is activated (deposited) at around ∼58 s. When activating the first element of the second layer, point A is within close proximity of the heat source. The same is true when activating the first elements of third, fourth, and fifth layers. However, when the last element is activated at the fifth layer, the laser processing stops and there is no more heat input, which increases the cooling rate and leads to a less colony—α content as shown in Fig. 12. The same applies to all probed points above A on the other layers.

To illustrate the peculiarity of this behavior to the last deposition point, i.e., point A, temperature profile for point B shown in Fig. 13(*a*) is presented in Fig. 13(*c*). Similarly, the times at which the temperature crosses T_β^{trans} and T_{IG} during cooling are marked in the figure. Since the uniformity of boundary conditions for this point throughout the process, the time spent for cooling as well as the amount of colony—α increase monotonically (up to 40%) throughout the process.

The cooling rate of 410 °C/s is used in most of the model as a threshold value for starting martensitic transformations [34,54–56,62]. The cooling rates below martensite start temperature (800 °C) do not exceed 410 °C/s in the calculated thermal history (e.g., Fig. 12). Hence, it is not necessary to consider martensitic phase transformation in the model. On the other hand, some processing parameters may cause high cooling rates (greater than 410 °C/s) during LENS process. At this point, the martensitic phase transformation can be easily included in the present model by using the formulation given in Ref. [53].

In the current research, several thermal-mechanical-microstructural interactions with relatively negligible effects on microstructural behavior are not considered (i.e., weak coupling) in order to simplify the model and optimize computational efficiency [58,59]. On the other hand, the microstructural model can be coupled with the thermal-mechanical models in order to establish a more accurate model and predict the material response (i.e., distortions and stresses) due to microstructure and temperature [17,20]. For instance, flow stress is also strongly influenced by microstructure besides strain, strain rate, and temperature. At this point, flow behavior of Ti-6Al-4V can be calculated using phase fraction information and the constitutive relations for each phase [17,54].

The density type microstructural modeling approach, which provides calculation of different phase fractions during the LENS process, is developed and coupled to the thermal model. However, the microstructure evolution of solidification during the LENS process is not considered in the model. At this point, the proposed thermal model can be modified and coupled with the microstructural models in order to predict different microstructural outputs such as nucleation sites, growth orientation, and grain growth during the solidification of Ti-6Al-4V [35,65].

4 Conclusions

A thermal-microstructural model for the LENS process of Ti-6Al-4V is presented and its implementation is described

comprehensively. The proposed model couples the heat transfer calculations with phase transformation kinetics. The thermal model is developed using FE method and validated through comparisons with pointwise temperature history measurements at different points on substrate. The microstructural model is developed by considering different kinetic models in the literature and coupled the thermal FE model via a written subroutine. The microstructural model is also verified and validated with numerical results in the literature and experimental measurements of lath width. The formation/dissolution of α-phases and β-phase, and α lath width evolution during heating and cooling cycles in LENS process are examined in detail. The simulation results showed that varying thermal histories along the height of the deposition lead to varying microstructures. It is observed that Widmanstätten colony and basketweave α-phase fractions significantly change during and after deposition process depending on the position of the heat source, hatching pattern, and the geometry of the deposited sample. It can be concluded that the proposed FE-based thermal-microstructural modeling approach is able to predict the microstructure evolution of Ti-6Al-4V during the LENS process and can help select the optimum process parameters to yield the desired microstructure and mechanical properties of the AM parts. The effects of processing parameters (i.e., scanning speed and orientation, laser power, layer thickness, numbers of layer, dwell time, and hatching pattern) on microstructural behavior of material have not been examined in this study. In addition, only lath width results are used to validate the model due to difficulty arising from distinguishing the α-phases. In the future, the effects of processing parameters on microstructural behavior of material will be also investigated systematically and the model validation will be improved by using different characterization techniques (tunneling electron microscope and X-ray measurements).

Acknowledgment

The first author (C.B.) was supported by The Scientific and Technological Research Council of Turkey (TUBITAK) within the context of 2219-Post Doctoral Fellowship Program.

Funding Data

- National Science Foundation (Grant No. CMMI-1434077).

References

[1] Murr, L. E., Gaytan, S. M., Ramirez, D. A., Martinez, E., Hernandez, J., Amato, K. N., Shindo, P. W., Medina, F. R., and Wicker, R. B., 2012, "Metal Fabrication by Additive Manufacturing Using Laser and Electron Beam Melting Technologies," J. Mater. Sci. Technol., **28**(1), pp. 1–14.
[2] Sandia National Laboratories, 2002, "Laser Engineered Net Shaping, Manufacturing Technologies," Sandia National Laboratories, Albuquerque, NM, accessed Sept. 15, 2017, http://www.sandia.gov/mst/pdf/LENS.pdf
[3] Mudge, R. P., and Wald, N. R., 2007, "Laser Engineered Net Shaping Advances Additive Manufacturing and Repair," Weld. J., **86**(1), pp. 44–48.
[4] Palčič, I., Balažic, M., Milfelner, M., and Buchmeister, B., 2009, "Potential of Laser Engineered Net Shaping (LENS) Technology," Mater. Manuf. Processes, **24**(7–8), pp. 750–753.
[5] Gu, D. D., Meiners, W., Wissenbach, K., and Poprawe, R., 2012, "Laser Additive Manufacturing of Metallic Components: Materials, Processes and Mechanisms," Int. Mater. Rev., **57**(3), pp. 133–164.
[6] Frazier, W. E., 2014, "Metal Additive Manufacturing: A Review," J. Mater. Eng. Perform., **23**(6), pp. 1917–1928.
[7] Guo, N., and Leu, M. C., 2013, "Additive Manufacturing: Technology, Applications and Research Needs," Front. Mech. Eng., **8**(3), pp. 215–243.
[8] Gibson, I., Rosen, D. W., and Stucker, B., 2010, *Additive Manufacturing Technologies*, Springer, New York.
[9] Thompson, S. M., Bian, L., Shamsaei, N., and Yadollahi, A., 2015, "An Overview of Direct Laser Deposition for Additive Manufacturing—Part I: Transport Phenomena, Modeling and Diagnostics," Addit. Manuf., **8**, pp. 36–62.
[10] Shamsaei, N., Yadollahi, A., Bian, L., and Thompson, S. M., 2015, "An Overview of Direct Laser Deposition for Additive Manufacturing—Part II: Mechanical Behavior, Process Parameter Optimization and Control," Addit. Manuf., **8**, pp. 12–35.
[11] Wu, X., Liang, J., Mei, J., Mitchell, C., Goodwin, P. S., and Voice, W., 2004, "Microstructures of Laser-Deposited Ti–6Al–4V," Mater. Des., **25**(2), pp. 137–144.
[12] Vastola, G., Zhang, G., Pei, Q. X., and Zhang, Y. W., 2016, "Modeling the Microstructure Evolution During Additive Manufacturing of Ti6Al4V: A Comparison Between Electron Beam Melting and Selective Laser Melting," JOM, **68**(5), pp. 1370–1375.
[13] Zhai, Y., Galarraga, H., and Lados, D. A., 2016, "Microstructure, Static Properties, and Fatigue Crack Growth Mechanisms in Ti-6Al-4V Fabricated by Additive Manufacturing: LENS and EBM," Eng. Failure Anal., **69**, pp. 3–14.
[14] Bian, L., Thompson, S. M., and Shamsaei, N., 2015, "Mechanical Properties and Microstructural Features of Direct Laser-Deposited Ti-6Al-4V," JOM, **67**(3), pp. 629–638.
[15] Marshall, G. J., Young, W. J., II, Thompson, S. M., Shamsaei, N., Daniewicz, S. R., and Shao, S., 2016, "Understanding the Microstructure Formation of Ti-6Al-4V During Direct Laser Deposition Via in-Situ Thermal Monitoring," JOM, **68**(3), pp. 778–790.
[16] Lundbäck, A., and Lindgren, L. E., 2011, "Modelling of Metal Deposition," Finite Elem. Anal. Des., **47**(10), pp. 1169–1177.
[17] Lindgren, L. E., Lundbäck, A., Fisk, M., Pederson, R., and Andersson, J., 2016, "Simulation of Additive Manufacturing Using Coupled Constitutive and Microstructure Models," Addit. Manuf., **12**(Part B), pp. 144–158.
[18] Goldak, J. A., and Akhlaghi, M., 2005, *Computational Welding Mechanics*, Springer Science & Business Media, New York.
[19] Lindgren, L. E., 2006, "Numerical Modelling of Welding," Comput. Methods Appl. Mech. Eng., **195**(48), pp. 6710–6736.
[20] Lindgren, L. E., 2007, *Computational Welding Mechanics: Thermomechanical and Microstructural Simulations*, Woodhead Publishing, Cambridge, UK.
[21] Anca, A., Fachinotti, V. D., Escobar-Palafox, G., and Cardona, A., 2011, "Computational Modelling of Shaped Metal Deposition," Int. J. Numer. Methods Eng., **85**(1), pp. 84–106.
[22] Costa, L., Vilar, R., Reti, T., and Deus, A. M., 2005, "Rapid Tooling by Laser Powder Deposition: Process Simulation Using Finite Element Analysis," Acta Mater., **53**(14), pp. 3987–3999.
[23] Wang, L., and Felicelli, S., 2006, "Analysis of Thermal Phenomena in LENS™ Deposition," Mater. Sci. Eng. A, **435–436**, pp. 625–631.
[24] Ye, R., Smugeresky, J. E., Zheng, B., Zhou, Y., and Lavernia, E. J., 2006, "Numerical Modeling of the Thermal Behavior During the LENS® Process," Mater. Sci. Eng. A, **428**(1), pp. 47–53.
[25] Peyre, P., Aubry, P., Fabbro, R., Neveu, R., and Longuet, A., 2008, "Analytical and Numerical Modelling of the Direct Metal Deposition Laser Process," J. Phys. D, **41**(2), pp. 1–10.
[26] Neela, V., and De, A., 2009, "Three-Dimensional Heat Transfer Analysis of LENS™ Process Using Finite Element Method," Int. J. Adv. Manuf. Technol., **45**(9–10), pp. 935–943.
[27] Zhu, G., Zhang, A., Li, D., Tang, Y., Tong, Z., and Lu, Q., 2011, "Numerical Simulation of Thermal Behavior During Laser Direct Metal Deposition," Int. J. Adv. Manuf. Technol., **55**(9–12), pp. 945–954.
[28] Fachinotti, V. D., Cardona, A., Baufeld, B., and Van der Biest, O., 2012, "Finite-Element Modelling of Heat Transfer in Shaped Metal Deposition and Experimental Validation," Acta Mater., **60**(19), pp. 6621–6630.
[29] Zhang, Y., Yu, G., and He, X., 2012, "Numerical Study of Thermal History in Laser Aided Direct Metal Deposition Process," Sci. China Phys., Mech. Astron., **55**(8), pp. 1431–1438.
[30] Michaleris, P., 2014, "Modeling Metal Deposition in Heat Transfer Analyses of Additive Manufacturing Processes," Finite Elem. Anal. Des., **86**, pp. 51–60.
[31] Ding, J., Colegrove, P., Mehnen, J., Williams, S., Wang, F., and Almeida, P. S., 2014, "A Computationally Efficient Finite Element Model of Wire and Arc Additive Manufacture," Int. J. Adv. Manuf. Technol., **70**(1–4), pp. 227–236.
[32] Heigel, J. C., Michaleris, P., and Reutzel, E. W., 2015, "Thermo-Mechanical Model Development and Validation of Directed Energy Deposition Additive Manufacturing of Ti–6Al–4V," Addit. Manuf., **5**, pp. 9–19.
[33] Yang, Q., Zhang, P., Cheng, L., Min, Z., Chyu, M., and To, A. C., 2016, "Finite Element Modeling and Validation of Thermomechanical Behavior of Ti-6Al-4V in Directed Energy Deposition Additive Manufacturing," Addit. Manuf., **12**(Part B), pp. 169–177.
[34] Vastola, G., Zhang, G., Pei, Q. X., and Zhang, Y. W., 2016, "Controlling of Residual Stress in Additive Manufacturing of Ti6Al4V by Finite Element Modeling," Addit. Manuf., **12**(Part B), pp. 213–239.
[35] Zhang, J., Liou, F., Seufzer, W., and Taminger, K., 2016, "A Coupled Finite Element Cellular Automaton Model to Predict Thermal History and Grain Morphology of Ti-6Al-4V During Direct Metal Deposition (DMD)," Addit. Manuf., **11**, pp. 32–39.
[36] Grong, Ø., and Shercliff, H. R., 2002, "Microstructural Modelling in Metals Processing," Prog. Mater. Sci., **47**(2), pp. 163–282.
[37] Froes, F. H., and Dutta, B., 2014, "The Additive Manufacturing (AM) of Titanium Alloys," Adv. Mater. Res., **1019**, pp. 19–25.
[38] Kelly, S. M., 2004, "Thermal and Microstructure Modeling of Metal Deposition Processes With Application to Ti-6Al-4V," Ph.D. thesis, Virginia Polytechnic Institute and State University, Blacksburg, VA.
[39] Kelly, S. M., and Kampe, S. L., 2004, "Microstructural Evolution in Laser-Deposited Multilayer Ti-6Al-4V Builds—Part I: Microstructural Characterization," Metall. Mater. Trans. A, **35**(6), pp. 1861–1867.
[40] Kelly, S. M., and Kampe, S. L., 2004, "Microstructural Evolution in Laser-Deposited Multilayer Ti-6Al-4V Builds—Part II: Thermal Modeling," Metall. Mater. Trans. A, **35**(6), pp. 1869–1879.
[41] Kolmogorov, A. N., 1937, "On the Statistical Theory of the Crystallization of Metals," Bull. Acad. Sci. USSR, Math. Ser., **1**, pp. 355–359.
[42] Johnson, W. A., and Mehl, R. F., 1939, "Reaction Kinetics in Processes of Nucleation and Growth," Trans. AIME, **135**(8), pp. 416–458.

[43] Avrami, M., 1941, "Granulation, Phase Change, and Microstructure Kinetics of Phase Change—III," J. Chem. Phys., **9**(2), pp. 177–184.
[44] Sha, W., and Malinov, S., 2009, *Titanium Alloys: Modelling of Microstructure, Properties and Applications*, Woodhead Publishing, Cambridge, UK.
[45] Scheil, E., 1935, "Anlaufzeit der Austenitumwandlung," Arch. Eisenhüttenwes, **8**(12), pp. 564–567.
[46] Christian, J. W., 2012, *Theory of Phase Transformations in Metals and Alloys*, Newnes, Burlington, MA.
[47] Koistinen, D. P., and Marburger, R. E., 1959, "A General Equation Prescribing the Extent of the Austenite-Martensite Transformation in Pure Iron-Carbon Alloys and Plain Carbon Steels," Acta Metall., **7**(1), pp. 59–60.
[48] Mur, F. G., Rodriguez, D., and Planell, J. A., 1996, "Influence of Tempering Temperature and Time on the α'-Ti-6Al-4V Martensite," J. Alloys Compd., **234**(2), pp. 287–289.
[49] Ahmed, T., and Rack, H. J., 1998, "Phase Transformations During Cooling in $\alpha+\beta$ Titanium Alloys," Mater. Sci. Eng. A, **243**(1), pp. 206–211.
[50] Elmer, J. W., Palmer, T. A., Babu, S. S., Zhang, W., and DebRoy, T., 2004, "Phase Transformation Dynamics During Welding of Ti–6Al–4V," J. Appl. Phys., **95**(12), pp. 8327–8339.
[51] Charles, C., 2008, "Modelling Microstructure Evolution of Weld Deposited Ti-6Al-4V," Master's thesis, Luleå University of Technology, Luleå, Sweden.
[52] Charles, C., and Järvstråt, N., 2009, "Modelling Ti–6Al–4V Microstructure by Evolution Laws Implemented as Finite Element Subroutines: Application to TIG Metal Deposition," Eighth International Conference on Trends in Welding Research (TWR), Pine Mountain, GA, June 1–6, pp. 477–485.
[53] Murgau, C. C., Pederson, R., and Lindgren, L. E., 2012, "A Model for Ti–6Al–4V Microstructure Evolution for Arbitrary Temperature Changes," Modell. Simul. Mater. Sci. Eng., **20**(5), p. 055006.
[54] Fan, Y., Cheng, P., Yao, Y. L., Yang, Z., and Egland, K., 2005, "Effect of Phase Transformations on Laser Forming of Ti–6Al–4V Alloy," J. Appl. Phys., **98**(1), p. 013518.
[55] Crespo, A., and Vilar, R., 2010, "Finite Element Analysis of the Rapid Manufacturing of Ti–6Al–4V Parts by Laser Powder Deposition," Scr. Mater., **63**(1), pp. 140–143.
[56] Crespo, A., 2011, *Convection and Conduction Heat Transfer*, INTECH Open Access Publisher, Rijeka, Croatia, Chap. 15.
[57] Suárez, A., Tobar, M. J., Yáñez, A., Pérez, I., Sampedro, J., Amigó, V., and Candel, J. J., 2011, "Modeling of Phase Transformations of Ti6Al4V During Laser Metal Deposition," Phys. Procedia, **12**(Part A), pp. 666–673.
[58] Irwin, J., Reutzel, E. T., Michaleris, P., Keist, J., and Nassar, A. R., 2016, "Predicting Microstructure From Thermal History During Additive Manufacturing for Ti-6Al-4V," ASME J. Manuf. Sci. Eng., **138**(11), p. 111007.
[59] Marion, G., Cailletaud, G., Colin, C., and Mazière, M., 2014, "A Finite Element Model for the Simulation of Direct Metal Deposition," 33rd International Congress on Applications of Lasers & Electro-Optics (ICALEO), San Diego, CA, Oct. 19–23, Paper No. 1801.
[60] Goldak, J., Chakravarti, A., and Bibby, M., 1984, "A New Finite Element Model for Welding Heat Sources," Metall. Trans. B, **15**(2), pp. 299–305.
[61] Gil, F., Ginebra, M., Manero, J., and Planell, J., 2001, "Formation of a-Widmanstatten Structure: Effects of Grain Size and Cooling Rate on the Widmanstatten Morphologies and on the Mechanical Properties in Ti6Al4V Alloy," J. Alloys Compd., **329**(1), pp. 142–152.
[62] Gong, X., Lydon, J., Cooper, K., Chou, K., and Branch, N., 2013, "Microstructural Characterization and Modeling of Beam Speed Effects on Ti-6Al-4V by Electron Beam Additive Manufacturing," 25th International of Solid Freeform Fabrication Symposium (SFF), Austin, TX, Aug. 4–6, pp. 459–469.
[63] Farrar, P. A., and Margolin, H., 1961, "The Titanium Rich Region of the Titanium-Aluminum-Vanadium System," Trans. AIME, **221**, pp. 1214–1221.
[64] Rasband, W. S., 2016, "ImageJ," U. S. National Institutes of Health, Bethesda, MD, accessed Sept. 10, 2017, https://imagej.nih.gov/ij/
[65] Sahoo, S., and Chou, K., 2016, "Phase-Field Simulation of Microstructure Evolution of Ti–6Al–4V in Electron Beam Additive Manufacturing Process," Addit. Manuf., **9**, pp. 14–24.